NASA/TM-20250009318

Real-Time Fourier Background-Oriented Schlieren

Mark P. Wernet
Glenn Research Center, Cleveland, Ohio

December 2025

NASA STI Program Report Series

Since its founding, NASA has been dedicated to the advancement of aeronautics and space science. The NASA scientific and technical information (STI) program plays a key part in helping NASA maintain this important role.

The NASA STI program operates under the auspices of the Agency Chief Information Officer. It collects, organizes, provides for archiving, and disseminates NASA's STI. The NASA STI program provides access to the NTRS Registered and its public interface, the NASA Technical Reports Server, thus providing one of the largest collections of aeronautical and space science STI in the world. Results are published in both non-NASA channels and by NASA in the NASA STI Report Series, which includes the following report types:

- TECHNICAL PUBLICATION. Reports of completed research or a major significant phase of research that present the results of NASA programs and include extensive data or theoretical analysis. Includes compilations of significant scientific and technical data and information deemed to be of continuing reference value. NASA counterpart of peer-reviewed formal professional papers but has less stringent limitations on manuscript length and extent of graphic presentations.

- TECHNICAL MEMORANDUM. Scientific and technical findings that are preliminary or of specialized interest, e.g., quick release reports, working papers, and bibliographies that contain minimal annotation. Does not contain extensive analysis.

- CONTRACTOR REPORT. Scientific and technical findings by NASA-sponsored contractors and grantees.

- CONFERENCE PUBLICATION. Collected papers from scientific and technical conferences, symposia, seminars, or other meetings sponsored or cosponsored by NASA.

- SPECIAL PUBLICATION. Scientific, technical, or historical information from NASA programs, projects, and missions, often concerned with subjects having substantial public interest.

- TECHNICAL TRANSLATION. English-language translations of foreign scientific and technical material pertinent to NASA's mission.

Specialized services also include organizing and publishing research results, distributing specialized research announcements and feeds, providing information desk and personal search support, and enabling data exchange services.

For more information about the NASA STI program, see the following:

- Access the NASA STI program home page at http://www.sti.nasa.gov

NASA/TM-20250009318

Real-Time Fourier Background-Oriented Schlieren

Mark P. Wernet
Glenn Research Center, Cleveland, Ohio

National Aeronautics and
Space Administration

Glenn Research Center
Cleveland, Ohio 44135

December 2025

Acknowledgments

This RT-F-BOS development work was supported by the Transformational Tools and Technology (TTT) Project of the Transformative Aeronautics Concepts Program (TACP). Operation of the Nozzle Acoustic Test Rig (NATR) was supported by James Bridges and the Commercial Supersonics Technology (CST) Project. Thanks to Puja Upadhyay and Heath Reising for providing the processed particle image velocimetry (PIV) results from the plug nozzle test hardware. The author would also like to thank the team at the Aero-Acoustic Propulsion Laboratory (AAPL) for their assistance in model setup and expertise in operating the NATR facility.

This work was sponsored by the
Transformative Aeronautics Concepts Program.

Level of Review: This material has been technically reviewed by technical management.

This report is available in electronic form at https://www.sti.nasa.gov/ and https://ntrs.nasa.gov/

NASA STI Program/Mail Stop 050
NASA Langley Research Center
Hampton, VA 23681-2199

Real-Time Fourier Background-Oriented Schlieren

Mark P. Wernet
National Aeronautics and Space Administration
Glenn Research Center
Cleveland, Ohio 44135

Summary

Background-oriented schlieren (BOS) is a widely used diagnostic for visualizing density gradients in high-speed aerospace flows. Conventional BOS implementations employ a camera to image a speckle background, with density gradients in the flow distorting the recorded pattern. These distortions are typically resolved using cross-correlation algorithms adapted from particle image velocimetry (PIV). Results are robust, but spatial resolution is limited and computational cost is high. In contrast to conventional approaches, the fast checkerboard demodulation (FCD) method uses a sinusoidal background pattern to isolate distinct frequency bands, enabling an alternative Fourier-based processing approach. This report presents real-time Fourier BOS (RT-F-BOS), a full real-time implementation of the FCD technique. Unlike earlier real-time BOS systems that relied on graphics processing unit (GPU) acceleration, RT-F-BOS delivers pixel-level density gradient estimates directly on multicore central processing units (CPUs), with the option to use GPUs for further speedup. This approach simplifies hardware requirements while maintaining high spatial resolution, providing a practical and efficient tool for real-time flow diagnostics in aerospace ground test facilities. A video attached to this report, TM-20250009318-Video.mp4, demonstrates the RT-F-BOS system in operation with a plug nozzle test article in the Glenn Research Center’s Nozzle Acoustic Test Rig (NATR).

Nomenclature

2D	two-dimensional
AAPL	Aero-Acoustic Propulsion Laboratory
CMOS	complementary metal-oxide-semiconductor
CPU	central processing unit
FCD	fast checkerboard demodulation
FFT	fast Fourier transform
FM	frequency modulation
FOV	field of view
GigE	Gigabit Ethernet interface
GPU	graphics processing unit
MKL	Math Kernel Library
NATR	Nozzle Acoustic Test Rig
NPR	nozzle pressure ratio
PIV	particle image velocimetry
RT-BOS	real-time background-oriented schlieren
RT-F-BOS	real-time Fourier background-oriented schlieren
SAFS	self-aligned focusing schlieren

Subscripts

b	bypass
c	core

Introduction

The background-oriented schlieren (BOS) technique is a widely adopted method for visualizing density gradients in high-speed and high-temperature flow fields. In supersonic applications, the most critical flow features of interest are the location and structure of shocks. BOS operates on principles similar to classic knife-edge schlieren but avoids its most demanding optical requirements. Classic schlieren requires large-diameter mirrors to collimate the illumination as well as high-quality optical windows in the wind tunnel walls (Ref. 1). BOS, in contrast, uses a much simpler optical arrangement with less stringent requirements on optical glass quality along the imaging path (Figure 1). An additional advantage is that BOS provides both the x- and y-components of the density gradient field, whereas knife-edge schlieren typically captures only a single component (Ref. 2). While classic schlieren inherently provides real-time visualization, most BOS systems have historically lacked online feedback. To address this limitation, real-time BOS (RT-BOS) implementations have been developed in which graphics processing unit (GPU) accelerated cross-correlation processing yields two-dimensional (2D) density gradient fields at resolutions comparable to those obtained in particle image velocimetry (PIV) (Refs. 3 and 4).

In a conventional BOS experiment, a digital camera images a uniformly illuminated random-dot or speckled background. A reference, or "wind-off," image is first recorded in the absence of flow. When a density field is introduced, gradients in the flow distort the observed background pattern. These distorted images are analyzed by comparing them to the reference image using cross-correlation algorithms adapted from PIV. The processing yields density gradient estimates in both the x- and y-directions. A fundamental limitation of this approach, however, is the spatial resolution imposed by the interrogation window size—typically 16 by 16 pixels—resulting in spatial averaging of the gradients across those subregions. Alternative methods such as optical flow and least-squares matching can improve sensitivity and resolution, but their computational expense makes them impractical for real-time applications (Refs. 5 and 6).

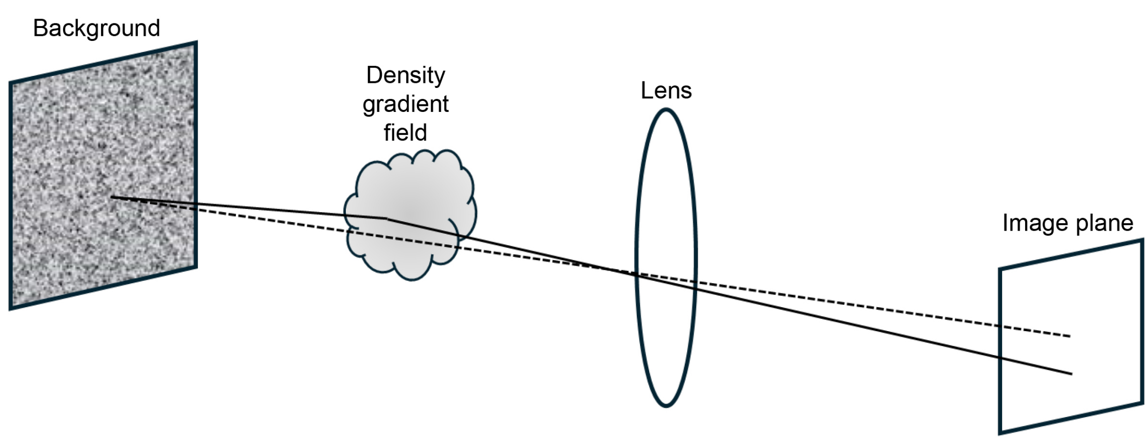

Figure 1.—Typical BOS layout showing speckle background, density gradient object, and imaging system.

Beyond BOS, other optical diagnostics have emerged with overlapping capabilities. Self-aligned focusing schlieren (SAFS) (Ref. 7), for example, shares many of BOS's advantages: it is simple to implement, requires only modest-quality windows, and is robust to vibrations. Unlike BOS, it requires no postprocessing and directly provides live schlieren data that can be captured with high-speed cameras. However, SAFS relies on polarization optics and thus cannot be used through birefringent windows—a restriction not encountered by BOS. More recently, event-based cameras have been applied to BOS (Ref. 8). By updating only pixels that change relative to the previous frame, these cameras enable extremely high effective frame rates. Yet, because the event-based cameras reference changes only to prior frames rather than an absolute baseline, reconstructing the images and extracting the density gradient fields is computationally complex.

The adaptability of BOS has driven its use across an expanding range of applications. In enclosed wind tunnels, artificial speckle backgrounds are readily generated, and in outdoor or full-scale tests of rotorcraft and aircraft, naturally occurring features such as tree canopies, desert terrain, or even the solar surface have been successfully exploited as stationary patterns (Refs. 9 and 10). The key requirement is that the background remain unchanged during measurements. For indoor applications, high-contrast speckle fields are typically created by spraying white dots on a dark surface. The size and density of these speckles strongly influence sensitivity, with optimal performance achieved when each speckle spans 2 to 3 pixels on the camera sensor (Ref. 2). This requirement often necessitates tailoring the background pattern to the specific field of view (FOV). Equally important is uniform, glare-free illumination, which can be challenging in large facilities with limited optical access.

To mitigate these practical challenges, high-definition monitors (3,840 by 2,160 pixels) have been employed to digitally generate speckle backgrounds in real-time BOS systems (Refs. 3 and 4). In the present work, high-definition monitors are again utilized, this time to display sinusoidal background patterns required by the fast checkerboard demodulation (FCD) approach (Ref. 11). While GPU-enhanced cross-correlation processing has been highly valuable for real-time BOS, enabling live feedback and dynamic control of facility operating conditions, the method remains constrained by its reliance on spatially averaged density gradients. With an effective resolution of a roughly 16- by 16-pixel grid, real-time methods struggle to capture fine-scale flow features. The FCD approach directly addresses this limitation, enabling real-time BOS processing without the need for GPU acceleration while providing single-pixel spatial resolution. A video supplement to this paper, TM-20250009318-SUPPL.mp4, demonstrates RT-F-BOS with a plug nozzle test article in the Glenn Research Center's Nozzle Acoustic Test Rig (NATR).

Fast Checkerboard Demodulation

The FCD technique employs a specially designed background pattern that allows for direct signal extraction (Ref. 11) . The pattern is a high-frequency, 2D checkerboard or sinusoidal pattern (see Figure 2), which acts like a carrier wave, similar to how FM (frequency modulation) works in radio. Density gradients in the test article (flow) distort the image recorded by the camera, thereby modulating the phase of the recorded checkerboard pattern. Proper selection of the sinusoidal pattern relative to the strength of the density gradients enables Fourier-based demodulation techniques to extract the density gradients relative to the reference image. By using a 2D checkerboard pattern, passbands in both the vertical and horizontal directions are generated, which enables displacements in the x- and y-directions to be extracted.

The 2D sinusoidal background pattern produces distinct carrier bands in the Fourier domain. These bands provide a basis for defining carrier passbands, whose locations are determined by the spatial frequency of the sinusoid, as shown in Figure 3. The passbands are typically defined as circular regions centered on the x- and y-direction carrier frequencies. Their radii are chosen to ensure adequate separation while preventing overlap between adjacent bands.

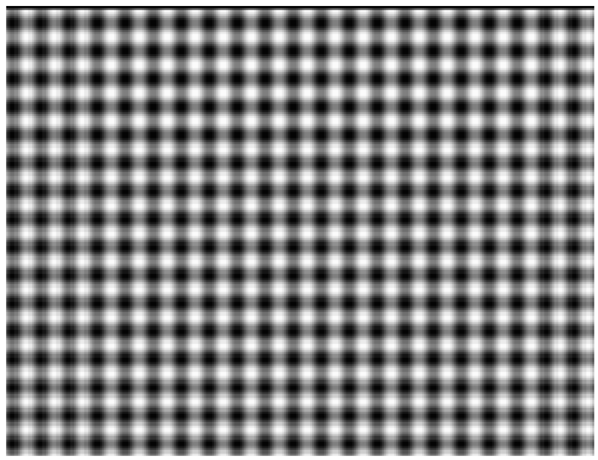

Figure 2.—Sinusoidal background used in FCD.

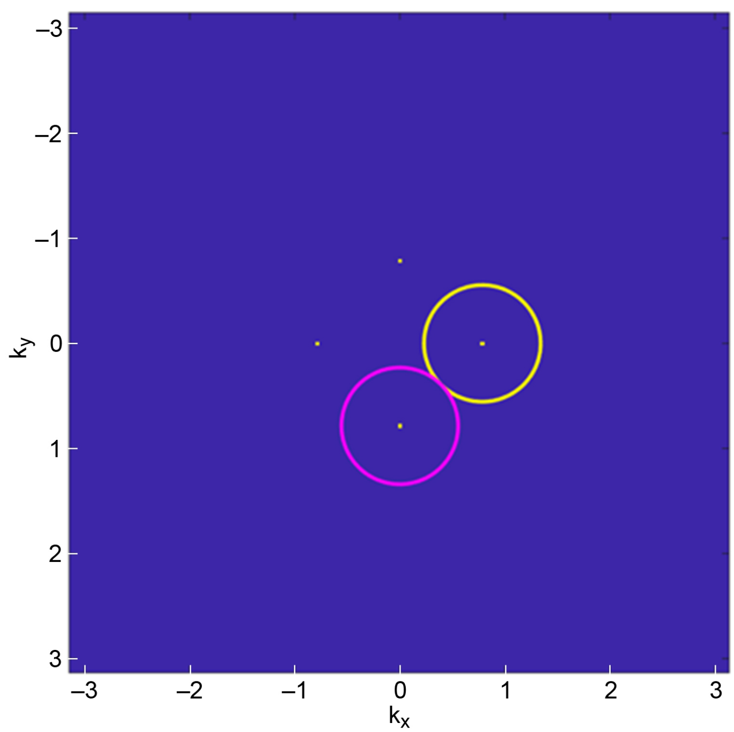

Figure 3.—Centered FFT of sinusoidal background; x- and y-direction circular passbands shown as yellow and magenta circles, respectively.

When the reference pattern contains only a 2D sinusoidal pattern, the reconstructed density field is free of any aberrations or leakage. If, however, there are any objects in the camera FOV, or the 2D sinusoid does not fill the entire camera FOV, then there can be substantial “ringing” in the reconstructed density field. The ringing contaminates the reconstructed density fields, undermining the quality of the result. Wildeman (Ref. 11) proposed that the ringing could be mitigated by interpolating the 2D sinusoidal pattern and filling in the regions blocked by the object or missing regions of the sinusoidal pattern. In practice, this proved to be difficult, given that the camera image of the sinusoid may have distortions from either perspective or lens distortion, making accurately interpolating/extrapolating the 2D sinusoid impractical. An alternative method for removing the ringing in the processed density fields is proposed and demonstrated in the FCD Passband Filtering section of this report.

Real-Time FCD Implementation

In a previously studied real-time BOS system (Refs. 3 and 4), GPUs were used to perform the large number of 2D fast Fourier transforms (FFTs) required for cross-correlation processing. While GPUs could also be used for implementing a real-time FCD approach, the computational load for FCD is significantly lower than that of cross-correlation. Therefore, the objective in this work was to implement the FCD technique using only a multicore central processing unit (CPU) while still achieving processing rates exceeding 10 frames per second (fps). The real-time processing code was written in C++ and utilized the Intel® (Intel Corp.) Math Kernel Library (MKL) optimized FFT routines.

A brief description of the FCD processing algorithm is provided here to outline the main processing steps and the number of complex 2D FFTs required to process each live image from the full-resolution Gigabit Ethernet (GigE) camera. A brief depiction of the salient processing steps in MATLAB® (The MathWorks, Inc.) syntax is shown in the Appendix. More detailed information on the FCD technique can be found in Wildeman (Ref. 11).

The first step, performed offline, is to extract complex carrier signals in both the x- and y-directions from the reference image. A 2D FFT of the reference is computed, and the x-direction frequency-domain filter (circular passband) is applied. The result is then returned to the spatial domain using an inverse 2D FFT. The process is repeated with the y-direction filter to obtain the corresponding carrier signal. Together, the x- and y-direction carrier signals represent the undistorted background pattern and provide the necessary reference information for processing the live images.

Live images are then processed to resolve the density gradients in both the x- and y-directions. When a live (deformed) image is captured during flow, a 2D FFT is computed, and the x- and y-direction circular passband filters are applied in the frequency domain to isolate the relevant spectral components. The filtered spectra for each direction are then transformed back to the spatial domain using inverse 2D FFTs. The filtered live images are then multiplied by their corresponding complex-valued reference carrier signals. The resulting complex products are used to extract the phase shift between the real and imaginary components, which indicates how much the background pattern has been displaced by density gradients in the flow. These phase shifts correspond to displacements in the horizontal (x) and vertical (y) directions. The total displacement magnitude is then computed from these two directional components.

Each live image in the RT-F-BOS system requires one forward 2D FFT and two inverse 2D FFTs as part of the FCD processing pipeline. Although the implementation utilizes the Intel® MKL FFT routines, the large image size (5 MP) results in a substantial computational load. Notably, within the Microsoft® Visual Studio® (Microsoft Corp.) environment, the Intel® MKL FFT routines do not inherently support multithreaded execution, limiting their performance on multicore systems. To overcome this, a custom hand-coded, parallelized, and multithreaded 2D FFT routine was developed, resulting in a 30%

improvement in processing speed. Additional multithreaded routines were also implemented for complex image array multiplications, further enhancing overall throughput. With these optimizations, the RT-F-BOS system successfully achieves acquisition, processing, and real-time display of 2,448- by 2,024-pixel images at 13 fps on an Intel® Xeon® (Intel Corp.) E5-2696 V4 processor with 22 physical cores.

The RT-F-BOS code allows live display of the processed images while simultaneously streaming the images to disk for later offline processing. Postprocessing of the images streamed to disk enables building movies of changes in the flow and for computation of mean density gradient fields for improved clarity. From the program dialog, the user can select which individual density component is displayed or the density gradient magnitude (see Figure 4). Three different colormaps are available for changing the displayed density gradient maps. The user can also set the width of the Gaussian passband filter to avoid overlapping passbands. An offset correction of the live camera image relative to the reference image is also selectable, where a cross-correlation of a small subregion of the image is used to compute and then implement any required subpixel image shift from vibration or thermal growth.

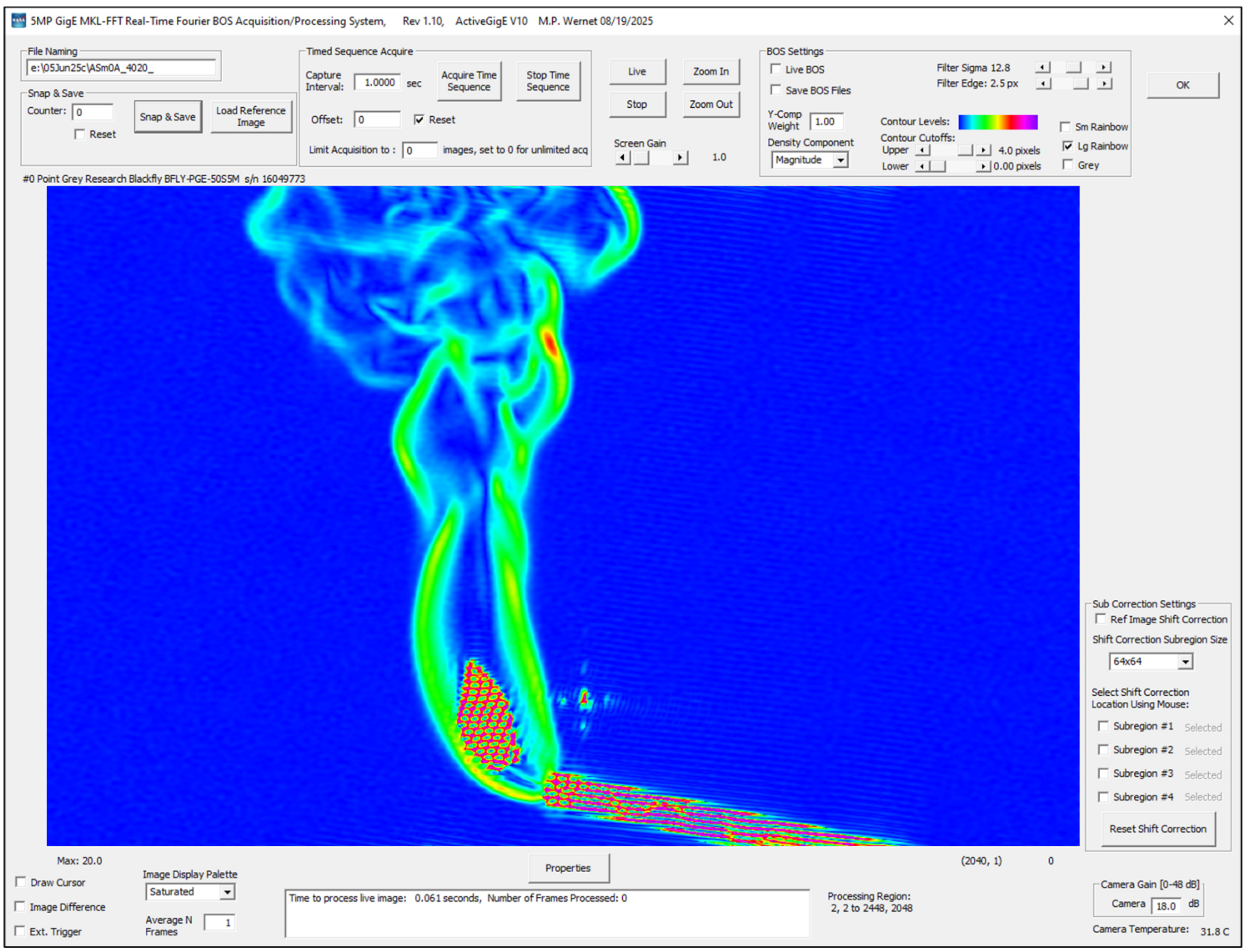

Figure 4.—Screenshot of RT-F-BOS dialog showing processed density gradient map and user controls. Use of uniform-intensity circular passbands results in ringing (light cyan-colored ripples) due to test article (butane lighter flame) in field of view.

The RT-F-BOS software package presented here provides an end-to-end solution for real-time acquisition, processing, and display through a graphical user interface. Wildeman's FCD paper (Ref. 11) also includes the term "real-time" in its title; however, the work primarily reports on processing throughput rather than demonstrating a fully integrated acquisition and processing system. The reported rates, 50 fps for 512- by 512-pixel images on a CPU and 190 fps on a GPU, appear to reflect processing of preacquired image frames, with no explicit discussion of live image acquisition. Details such as the camera used and real-time data handling procedures are not provided. The FCD algorithm itself produces a density gradient estimate at each image pixel. Based on the reported frame rates, the CPU processing corresponds to ~13.1 MP/s (512 by 512 by 50 fps), whereas the GPU rate corresponds to ~49.8 MP/s (512 by 512 by 190 fps). These figures represent only the processing step and do not account for image acquisition or image file transfer times.

In contrast, the RT-F-BOS system developed here performs live acquisition, real-time processing, and visualization of 2,448- by 2,024-pixel images at 13 Hz, achieving a total throughput of 64.9 MP/s. This includes the overhead of image acquisition, processing, and display—constituting a complete and demonstrable real-time BOS system.

FCD Passband Filtering

Ringing artifacts in the processed density gradient fields often arise when sharp-edged objects obscure the sinusoidal background pattern. In RT-F-BOS, introducing a model or object into the FOV after the reference image has been collected produces a "bleed-through" of the background in the masked regions. Figure 4 illustrates this effect, showing both the sinusoidal bleed-through (red sinusoid pattern) at the location of the object (a butane lighter and flame) and the lighter cyan ripples that appear above the flame and around the lighter body. Wildeman (Ref. 11) previously proposed mitigating the loss of carrier information in masked regions—caused by obstructions or areas where the background is not visible—by extrapolating the sinusoidal background into these regions. This is achieved by fitting a pattern to the visible portions of the reference image and extending it across the masked areas, thereby preserving continuity of the carrier signal for subsequent Fourier processing. However, in practice, extrapolating the sinusoidal background correction method proved difficult to implement, particularly in large-scale facility setups. In the optical system used in this work, for example, the camera was not perfectly perpendicular to the monitor, resulting in perspective distortion of the sinusoidal pattern. These distortions made accurate fitting and extrapolation of the background pattern into blocked/masked regions impractical. Additionally, optical aberrations from the camera lens can alter the periodicity of the recorded sinusoidal pattern, further complicating reconstruction.

To address this challenge, a modified version of the FCD filtering method was adopted. The original FCD approach employs unity-amplitude circular passbands in the frequency domain to isolate the horizontal and vertical carrier frequencies of the sinusoidal background. These unity-amplitude passbands have sharp edges that can introduce ringing artifacts due to the abrupt transition in frequency space. To suppress this effect, Gaussian smoothing was applied to the passband edges by convolving them with a Gaussian kernel, as illustrated in Figure 5. Line profiles through the center of the original circular unity-amplitude passband and the Gaussian-filtered passband illustrate the smoothing effect, while remaining within the original passband width. Also shown in Figure 5 are the 2D intensity contours of the unity-amplitude passband and the Gaussian-smoothed passband. This softening introduces a more gradual filter roll-off, attenuating the high-frequency components that contribute to ringing.

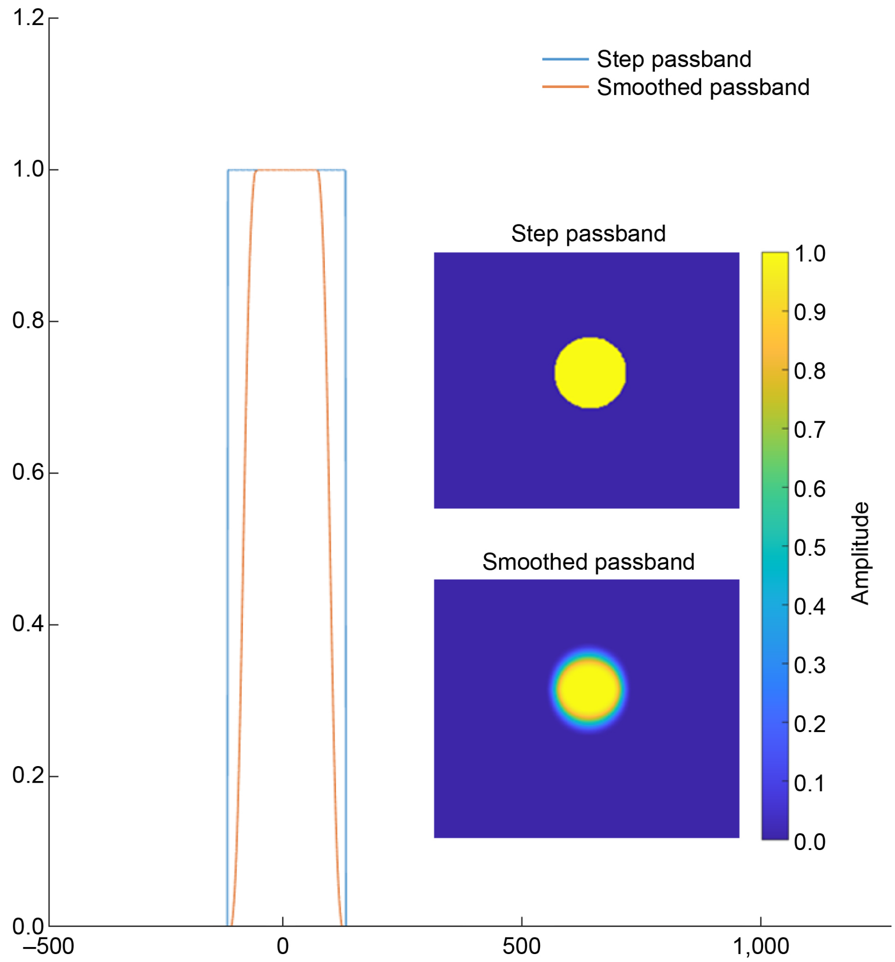

Figure 5.—Left, two line profiles through center of original unity-amplitude circular passband with line profile from smoothed, Gaussian-filtered passband. Right, corresponding 2D intensity maps comparing sharp-edged step passband with smoothed Gaussian-filtered version.

The degree of roll-off, however, must be carefully selected for each specific case. Excessive smoothing can lead to overlap between the horizontal and vertical passbands in the frequency domain, which may degrade the accuracy of the demodulation. To prevent this, it may be necessary to reduce the initial diameter of the circular passbands before applying Gaussian smoothing.

Nozzle Acoustic Test Rig

The demonstration test was conducted in the NASA Glenn Research Center's Aero-Acoustic Propulsion Laboratory (AAPL), a 65-ft-radius anechoic geodesic hemispherical dome (Ref. 12). The nozzles were mounted on a jet engine simulator, the Nozzle Acoustic Test Rig (NATR), contained in the AAPL. The NATR is a free jet wind tunnel, which provided the flight stream for the engine simulator. A turbofan engine simulator, the High Flow Jet Exit Rig, is fed by compressed air from centralized compressors, delivered to the test article through a system of manifolds, heaters, control valves, and flow conditioners. For setpoints simulating an aircraft engine, all air streams were preheated using a mixed-flow heat exchanger before being split into two streams, representing core and bypass streams on an engine and directed to coannular settling chambers in the rig. Both air streams were heated to the same temperature for this series of tests. Results from a plug-nozzle test article, shown in Figure 6, will be reported here.

RT-F-BOS Setup in NATR

The RT-F-BOS technique is relatively simple to set up, requiring just a camera and a monitor to be installed in the test rig. A 2,448- by 2,048-pixel complementary metal-oxide-semiconductor (CMOS) camera with a GigE interface was installed between acoustic-absorbing wedges in a vertical wall adjacent to the jet exit. The BOS camera imaged a 2D sinusoidal pattern displayed on a 218-cm (86-in.) diagonal high-definition monitor, positioned 8.2 m (27 ft) from the camera (see Figure 7). The frequency of the sinusoidal pattern was adjusted to minimize the background noise in the density gradient field while still

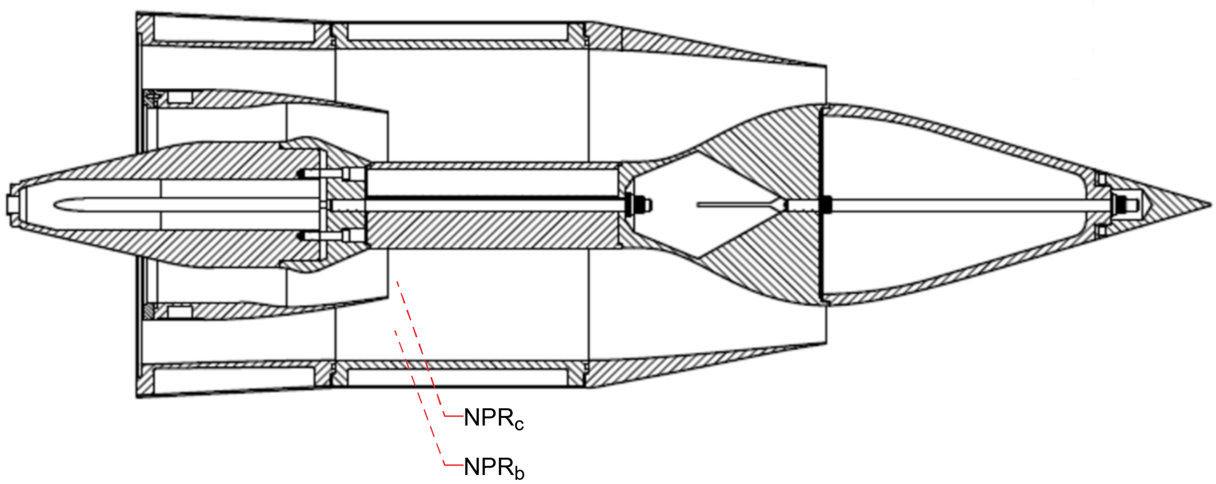

Figure 6.—Plug nozzle test article with two internal flow streams, run at equal temperature and pressure ratios.

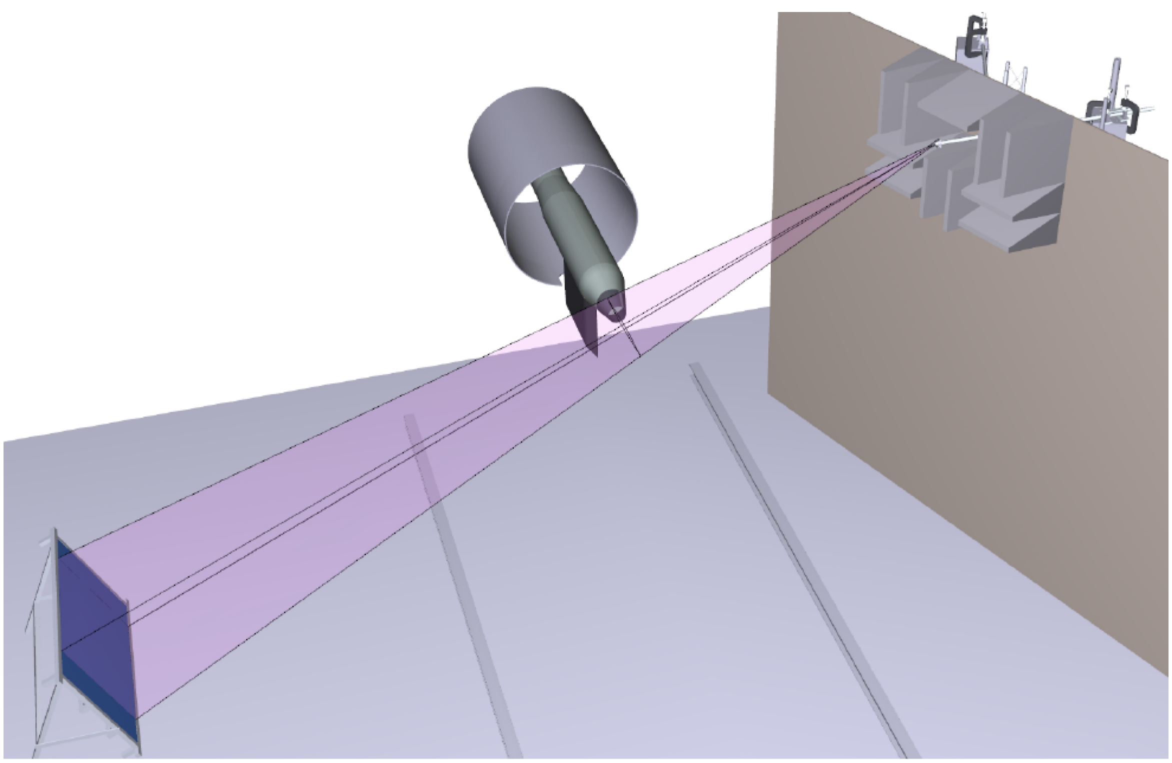

Figure 7.—CAD rendering of installation illustrating camera mounting location in wedge wall and monitor location on floor.

maintaining good sensitivity to density gradients. The monitor was mounted perpendicular to the plane of the overhead microphone array and tilted at a 25° angle from vertical. The camera itself was located approximately 3 m (9 ft) from the nozzle centerline. Live images from the BOS camera were acquired, processed, and displayed by a dedicated computer in the AAPL control room, approximately 91 m (300 ft) away, at a 13-Hz frame rate. To help prevent image blur due to vibrations, the camera mount was isolated from the wedge wall.

Results and Discussion

The primary objective of this study was to capture shock structures on the external plug surfaces and within the initial flow region of the internal plug configurations. Results presented here were obtained using model configuration 122DLm0Ap2069, which delineates the internal mixer and plug nozzle shape (Ref. 13). Sequences of 200 images were streamed to disk across eight different setpoints, as summarized in Table I. NPR_c denotes the pressure ratio of the inner annulus relative to ambient air, and NPR_b represents the pressure ratio of the outer annulus at the same axial location (Figure 6) to the ambient air. The temperature ratios, total temperature to ambient temperature, are defined at the same locations as the pressure ratios. Setpoint 7 represents a common rig condition used to evaluate consistency across different test programs in the AAPL.

Figure 8 compares 200-frame averaged density gradient magnitudes at setpoint 7 using two different processing methods. In Figure 8(a), the x- and y-component gradients are computed using standard FCD processing with uniform-intensity circular passbands. Figure 8(b) shows the relative density gradient magnitude obtained using Gaussian-filtered, rolled-off passbands. In both cases, the colormap represents the normalized density gradient magnitude, scaled by the maximum displacement.

Notable ringing artifacts appear in Figure 8(a), particularly in the flow region below the nozzle centerline. These are effectively suppressed in Figure 8(b) by the softened-edge passband, without degrading flow field features. All subsequent density gradient maps are processed using the Gaussian-filtered passbands. Additionally, although the hardware is nominally axisymmetric, the tested plug nozzle model exhibits asymmetry; the plug nozzle is slightly offset below the model centerline. This offset introduces asymmetries in the shock-filled flow field, which become more pronounced at higher nozzle pressure ratios (NPRs).

TABLE I.—RIG SETPOINTS FOR PLUG NOZZLE MODEL

Setpoint	NPR_c	NPR_b	T_{Tc}/T_{amb}	T_{Tb}/T_{amb}
7	1.856	1.856	1	1
4010	1.893	1.893	1	1
4020	1.915	1.915	1	1
4030	1.938	1.938	1	1
4040	1.984	1.984	1	1
4050	2.033	2.033	1	1
4060	2.083	2.083	1	1
4070	2.135	2.135	1	1

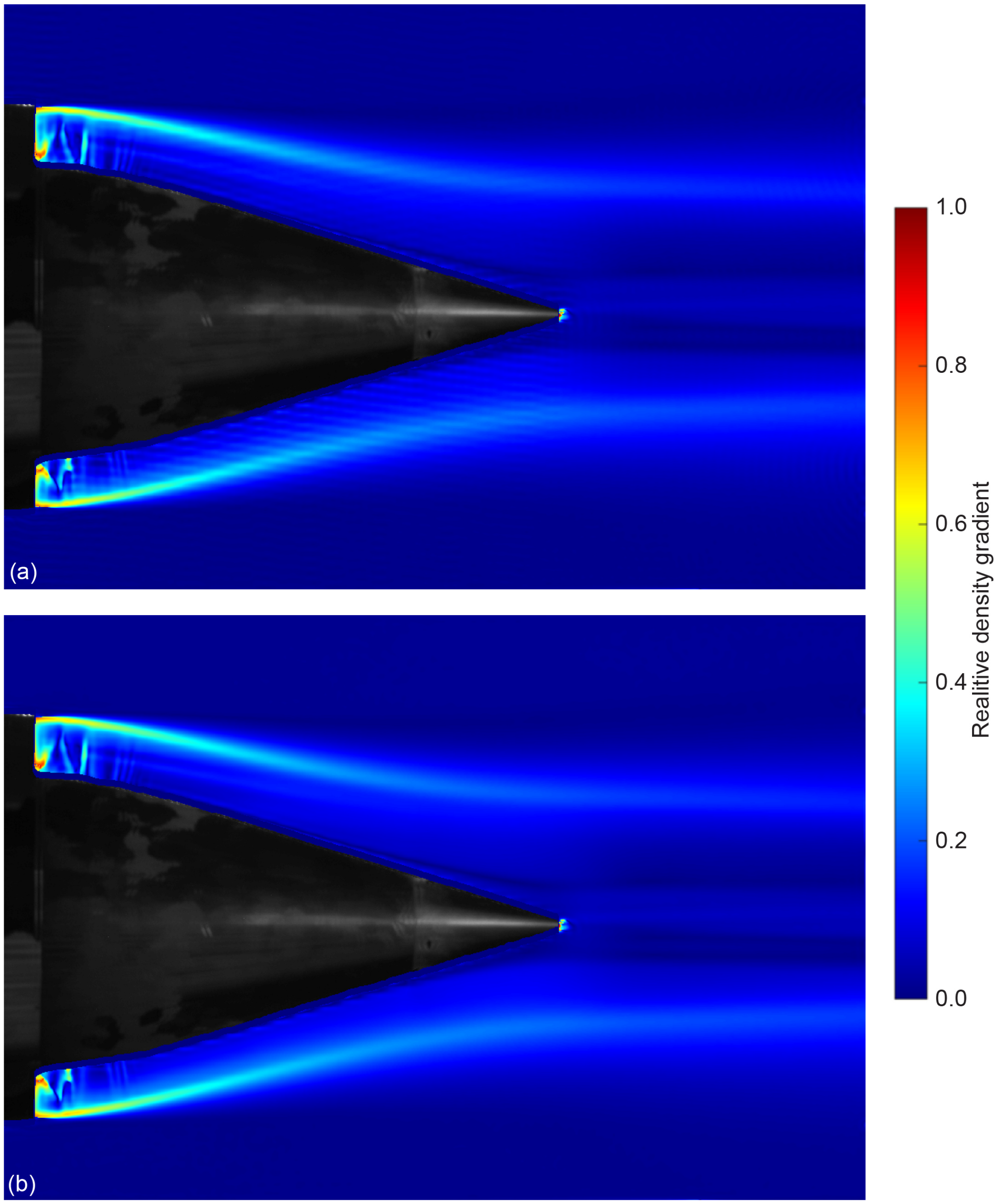

Figure 8.—Comparison of processed density gradient magnitude results; model image overdrawn to hide sinusoidal pattern bleed-through. (a) Uniform-intensity circular passband results. (b) Gaussian smoothed passband results where ringing on unfiltered case is removed with no loss of fidelity in features in flow.

Figure 9 presents the averaged density gradient magnitude maps for all eight rig setpoints listed in Table I. At the lowest setpoint, shocks are visible near the nozzle exit, where the plug shape is curved. As $NPR_{c,b}$ increases (setpoints 4010 to 4040), additional reflected shocks appear farther downstream, confined between the shear layer and the plug surface.

At setpoint 4050, reflected shocks extend along the full length of the plug. However, due to model asymmetry, the number of reflections differs between the upper and lower halves of the flow. At setpoint 4060, shocks extend beyond the plug’s end, but their asymmetry causes rapid decay downstream. By setpoint 4070, the shock trains in the upper and lower halves of the flow become more in-phase, resulting in a more coherent and sustained shock train beyond the nozzle plug.

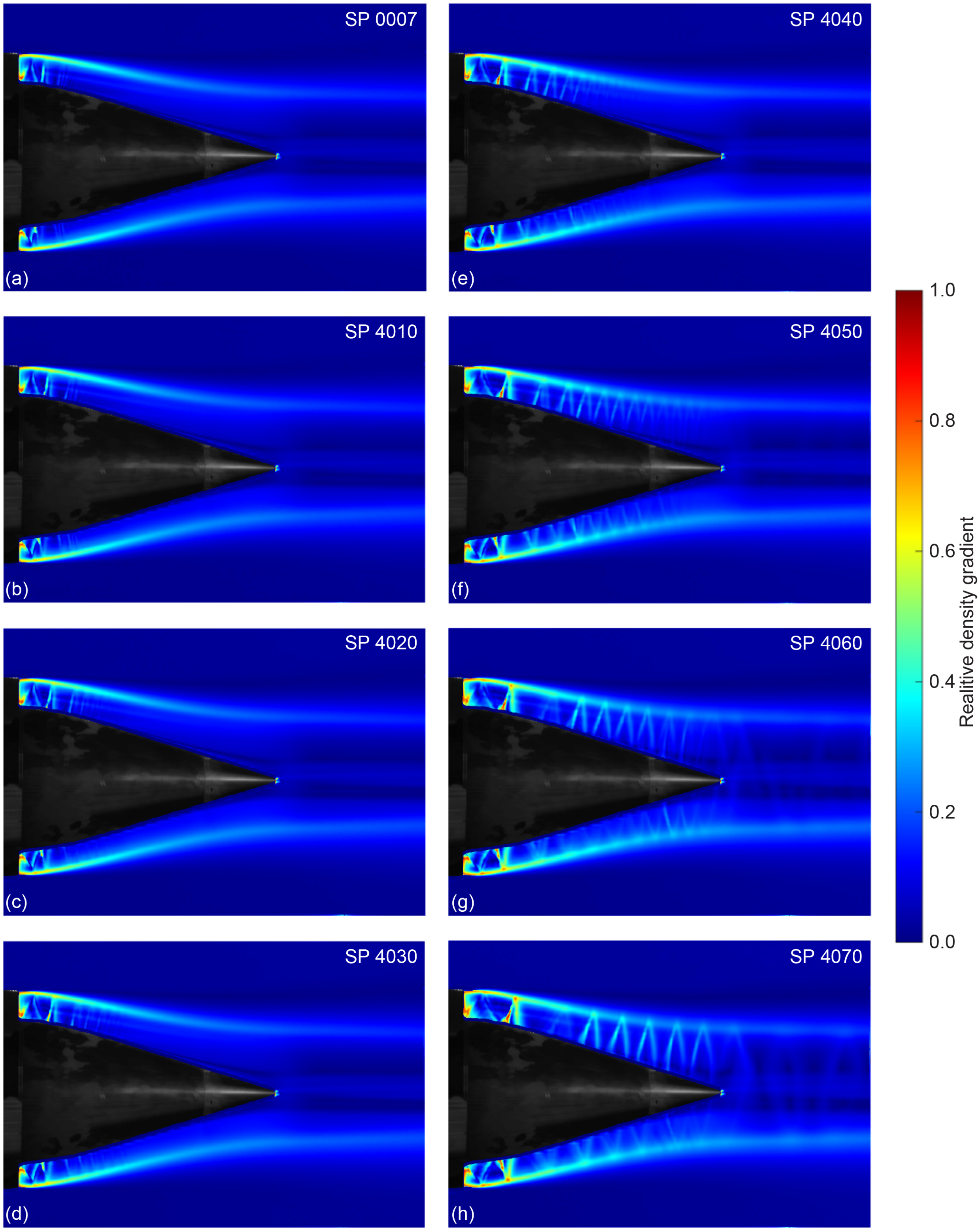

Figure 9.—Density gradient field across full test matrix, corresponding to Table I. (a) to (h) Setpoints 1 to 8.

During the test campaign, both PIV and RT-F-BOS measurements were collected, with this report focusing on the RT-F-BOS results. Figure 10 compares RT-F-BOS and PIV results at setpoint 7.

In the PIV setup, the laser light sheet enters from below the nozzle and is blocked by the plug, allowing measurement of only the lower half of the nozzle flow. However, the full vertical extent of the flow is captured downstream of the model. The PIV velocity data shown here was multipass processed down to a 16- by 16-pixel grid. Figure 10(a) presents the lower half of the RT-F-BOS results, providing a close-up view of the flow exiting the nozzle annulus. A strong, triangular shock is visible near the nozzle exit, followed by a series of weaker reflected shocks downstream.

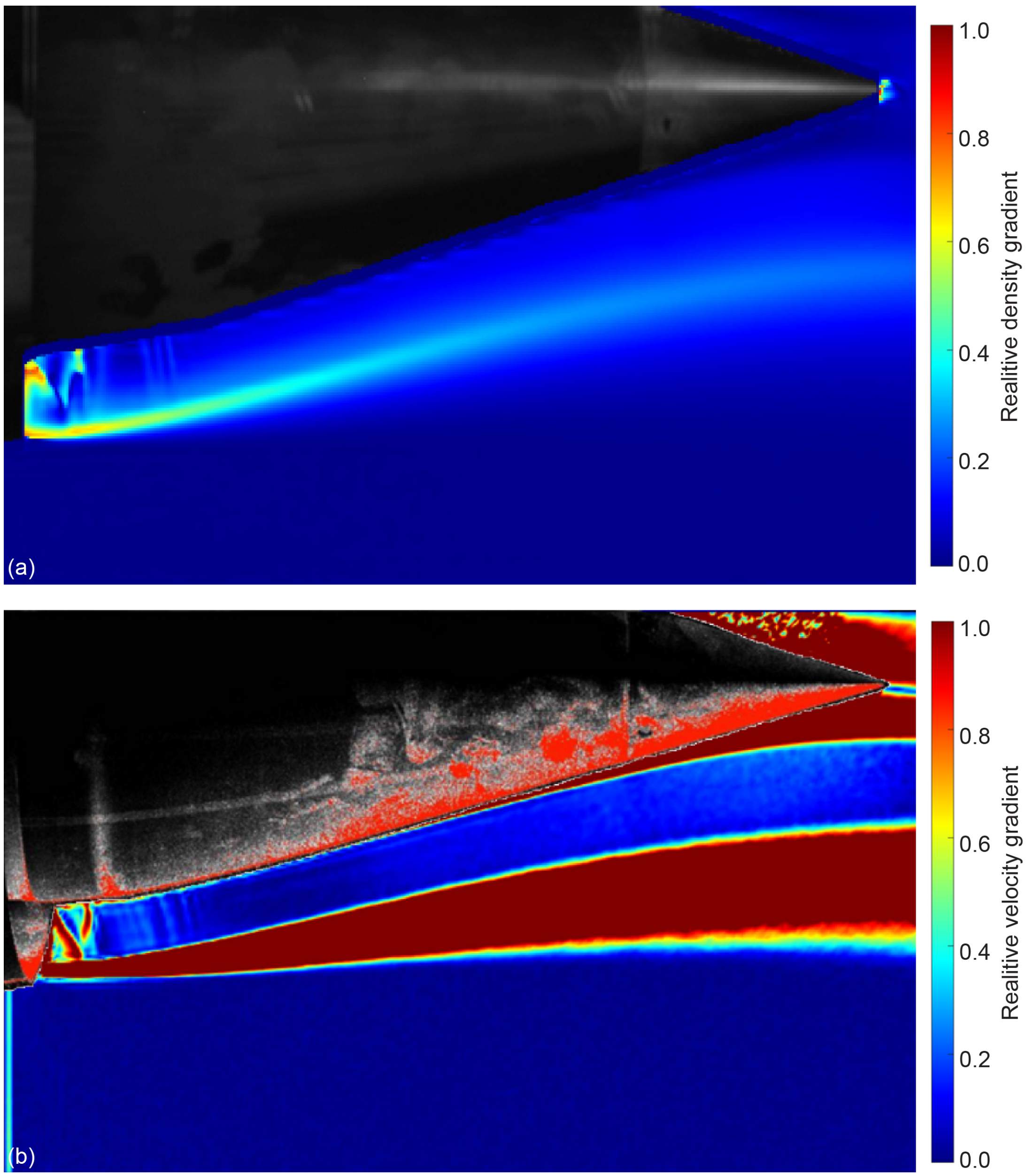

Figure 10.—Comparison of RT-F-BOS measured density gradient to derivative of PIV velocity measurements, both at setpoint 7. (a) RT-F-BOS case. (b) PIV case; colormap scale adjusted to visualize shocks near nozzle annulus.

Because the raw PIV velocity field does not clearly capture shock structures, the spatial derivatives of the *u*- and *v*-velocity components were used to compute a normalized velocity gradient magnitude, shown in Figure 10(b). The colormap was optimized to highlight weak shocks near the annulus exit, with the shear layer gradients saturated at the upper contour limit.

Focusing on the region between the shear layer and the plug surface, both techniques capture the same fundamental flow features: a strong initial shock followed by weaker reflections. However, RT-F-BOS offers substantially higher spatial resolution, providing a more detailed depiction of the shock structures along the nozzle plug surface.

In a video attached to this report, TM-20250009318-Video.mp4, the rig transitions from a high NPR to ambient conditions, transitioning across the complete range of setpoints listed in Table I and shown in Figure 9. The high NPR point in the video is actually above the setpoint value of 4070 listed in Table I. The RT-F-BOS measured density gradient magnitude is shown in the colormap, and the image sequence is displayed at 5 times the acquisition speed. Unique density gradients are shown at every pixel in the RT-F-BOS camera image. As the NPR is reduced, the complex shock train downstream of the nozzle collapses. Minor hardware imperfections introduce small asymmetries in the observed shock train structure just downstream of the nozzle plug.

Concluding Remarks

A real-time implementation of fast checkerboard demodulation (FCD) for background-oriented schlieren (BOS), termed RT-F-BOS, has been successfully developed and demonstrated in a large-scale aeroacoustics test facility. Unlike traditional cross-correlation BOS approaches that require graphics processing unit (GPU) acceleration and produce spatially averaged results, the RT-F-BOS method provides pixel-level density gradient estimates while maintaining real-time throughput on CPU-based systems. Optimized fast Fourier transform (FFT) routines and multithreading enable full-resolution (2,448- by 2,024-pixel) image acquisition, processing, and visualization at 13 Hz, representing a complete end-to-end system.

The use of Gaussian-smoothed passbands effectively mitigated ringing artifacts inherent in conventional FCD filtering, improving the clarity of reconstructed flow fields. Application of RT-F-BOS in the NASA Glenn Nozzle Acoustic Test Rig demonstrated its ability to capture detailed shock structures on nozzle plug surfaces, revealing flow asymmetries and evolution of reflected shock trains across a range of nozzle pressure ratios. Comparisons with particle image velocimetry (PIV) measurements confirmed that RT-F-BOS provides substantially higher spatial resolution of shock features with a simpler experimental setup.

Overall, RT-F-BOS offers a practical, robust, and high-resolution real-time diagnostic capability for aerospace ground test facilities. By eliminating GPU dependence, simplifying hardware requirements, and providing clear visualization of density gradients, the method enhances facility operations and broadens the applicability of BOS to a wider range of flow measurement problems.

Appendix

The fast checkerboard demodulation (FCD) processing steps are illustrated in general MATLAB® syntax.

1. Generate the x- and y-direction complex conjugate carrier signals from the reference image:

```
fftIref = fft2(Iref);                  % 2D FFT of reference image
ccX = conj(ifft2(fftIref .* CircX));   % CircX is the x-direction passband
ccY = conj(ifft2(fftIref .* CircY));   % CircY is the y-direction passband
```

ccX and ccY are the only information needed from the reference image. Next, each live density gradient deformed image is processed.

2. For each live image, take the 2D fast Fourier transform (FFT) of the live image and multiply by the circular passband in the x- and y-directions and then inverse transform.

```
fftIlive = fft2(Ilive)                 % 2D FFT of live image
Filt_LiveX = ifft2(fftIlive .* CircX) % Filter live image through x-passband
Filt_LiveY = ifft2(fftIlive .* CircY) % Filter live image through y-passband
```

3. Lastly, compute the phase shift in the product of the complex conjugate of the frequency-filtered reference image multiplied by the frequency-filtered live image.

```
Xdisp = -atan2(imag(Filt_LiveX .* ccX), real(Filt_LiveX .* ccX))
Ydisp = -atan2(imag(Filt_LiveY .* ccY), real(Filt_LiveY .* ccY))
```

For RT-F-BOS, the measured x- and y-displacements (X_{disp}, Y_{disp}) are limited to $\pm\pi$.

References

1. Settles, G. S., "Schlieren and shadowgraph techniques: Visualizing phenomena in transparent media," Springer-Verlag, ISBN 3-540-66155-7, 1949.
2. Raffel, M., "Background-oriented schlieren (BOS) techniques," Exp. Fluids 56:60, 2015. https://doi.org/10.1007/s00348-015-1927-5
3. Wernet, M. P., "Real-time background oriented schlieren: Catching up with knife edge schlieren," NASA Technical Report TM-2019-220144. https://ntrs.nasa.gov/citations/20190002831
4. Wernet, M. P., "Real-time background oriented schlieren with self-illuminated speckle background," Technical Note in Meas. Sci & Techn., Vol 31, No. 1, 2019. https://doi.org/10.1088/1361-6501/ab4211
5. Atcheson, B., Heidrich, W., and Ihrke, I. "An evaluation of optical flow algorithms for background oriented schlieren imaging," Exp. Fluids 46, 467–476 (2009). doi.org/10.1007/s00348-008-0572-7
6. Wang, Y., Li, B., Ding, Y., and He, H., "Remote sensing image matching algorithm based on the correlation coefficient-least square method," Proc. SPIE 12617, Ninth Symposium on Novel Photoelectronic Detection Technology and Applications, 126175K, April, 2023. https://doi.org/10.1117/12.2666545
7. Bathel, B. F., Boyda, M. T., and Weisberger, J. M., "Self-aligned focusing schlieren in optically constrained environments," Applied Optics, vol. 63, no. 26, p. 6831, 2024. https://doi.org/10.1364/AO.533087
8. Shiba, S., Hamann, F., Aoki, Y., and Gallego, G., "Event-based background-oriented schlieren," IEEE Transactions on Pattern Analysis and Machine Intelligence, Oct. 2023. doi.org/10.48550/arXiv.2311.00434
9. Hargather, M. J., and Settles, G. S., "Natural-background-oriented schlieren imaging," Exp. Fluids 48, pp. 59–68, 2010. https://doi.org/10.1007/s00348-009-0709-3
10. Heineck, J. T., Banks, D., Schairer, E. T., Haering, E. A., and Bean, P. "Background oriented schlieren (BOS) of a supersonic aircraft in flight," AIAA Flight Testing Conference, AIAA AVIATION Forum, (AIAA 2016-3356), 2016. https://doi.org/10.2514/6.2016-3356.
11. Wildeman, S., "Real-time quantitative Schlieren imaging by fast Fourier demodulation of a checkered backdrop," Exp. Fluids, 59:97, 2018. https://doi.org/10.1007/s00348-018-2553-9
12. Castner, R. S., "The Nozzle Acoustic Test Rig: An acoustic and aerodynamic free-jet facility," NASA TM 106495, 1994. https://ntrs.nasa.gov/citations/19940024246
13. Bridges, J., Podboy, G. G., and Wernet, M. P., "Plug20 test report," NASA/TM-20210010291, 2021. https://ntrs.nasa.gov/api/citations/20210010291/downloads/TM-20210010291.pdf